https://doi.org/10.5194/egusphere-2026-1170
Preprint. Discussion started: 24 March 2026

LaScape 1.0: An open-source module for three-dimensional thermo-mechanical and landscape evolution modeling

Yun Luo[1,2], Jianfeng Yang[1,2], Boris J. P. Kaus[3], Anton A. Popov[3], Shaohui Liu[1,2], Xiaoping Yuan[4], Liang Zhao[5,2]

[1]State Key Laboratory of Lithospheric and Environmental Coevolution, Institute of Geology and Geophysics, Chinese Academy of Sciences, Beijing, 100029, China
[2]College of Earth and Planetary Sciences, University of Chinese Academy of Sciences, Beijing, 100049, China
[3]Institute of Geosciences, Johannes Gutenberg University, Mainz, 55128, Germany
[4]School of Earth Sciences, China University of Geosciences, Wuhan, 430074, China
[5]Key Laboratory of Deep Petroleum Intelligent Exploration and Development, Institute of Geology and Geophysics, Chinese Academy of Sciences, Beijing, 100029, China

Correspondence to: Jianfeng Yang (yangjf@mail.iggcas.ac.cn)

Abstract. The feedback between tectonic events and surface processes fundamentally shapes landscapes and lithospheric deformation. However, the quantitative interaction remains poorly constrained. While numerical simulations offer powerful insights, 3D numerical models that couple thermo-mechanical processes with landscape processes remain uncommon due to the mismatches in temporal and spatial scales. Here, we present a 3D coupling module, LaScape, to integrate the thermo-mechanical code LaMEM with the landscape evolution code FastScape. A finite-difference marker-in-cell technique solves the thermo-mechanical processes, and a sticky air layer at the top boundary, combined with an internal mesh, effectively and stably simulates the free surface. Each timestep is synchronized with a finite-difference landscape evolution model. The timesteps of LaMEM are read by FastScape, which then subdivides them into smaller, iterative intervals to simulate surface processes. We demonstrate that the coupled model operates efficiently and stably. We validate our couple model by applying it to three classical tectonic regimes: oceanic subduction, continental collision, and continental extension. These cases converge quickly and align well with geologically realistic results. This approach provides a powerful, quantitative tool for exploring the bidirectional feedback mechanisms between the deep Earth and its surface, offering insights into the genesis of complex geological structures and landscapes.

1 Introduction

The dynamic interplay between tectonic events, climate, and surface processes fundamentally shapes Earth's topography (Molnar et al., 1993; Beaumont et al., 2001; Whipple, 2009). Crustal deformation via subduction, collision, and mantle dynamics shapes the surface topography, which in turn influences the climate, erosion-deposition processes, and river systems (Clark et al., 2004; Braun, 2010; Castelltort et al., 2012; Sacek et al., 2012; Cloetingh and Willett, 2013; Burov and Gerya,

https://doi.org/10.5194/egusphere-2026-1170
Preprint. Discussion started: 24 March 2026

2014; Replumaz et al., 2020; Yang et al., 2020a; Yuan et al., 2024; Borgohain et al., 2025; Xue et al., 2025). Surface processes may alter the crustal stress field through sedimentary loading and erosional unloading, thereby influencing the dynamics of the orogenic wedge, rifts, and fold-thrust belts (Burov and Cloetingh, 1997; Willett, 1999; Simpson, 2006; Bishop, 2007; Braun and Yamato, 2010; Wolf et al., 2022a; Wolf et al., 2022b; Li et al., 2025). Furthermore, weak and hot materials beneath the surface may move laterally or vertically due to isostasy. Areas experiencing rapid erosion can lead to the upwelling of warmer crustal materials, causing partial melting of rocks due to decompression and weakening of the crust, which may create tectonic weak zones (Beaumont et al, 2001; Zeitler et al., 2001; Koons et al., 2013; Yang et al., 2023). Besides, materials (e.g., rock, snow, water) loading and unloading can also cause spatio-temporal variations in Coulomb stress, which may accelerate or slow the rate of stress loading on active faults and further affect the time intervals between seismic events (Gao et al., 2000; Heki, 2003; Bettinelli et al., 2008; Liu et al., 2009).

There are increasing reports of interactions among tectonic, climate, and landscape systems; however, our quantitative understanding of these interactions remains limited. Numerical models have played a pivotal role in quantifying these couplings. Previous studies integrate surface processes and tectonics have been conducted to examine the evolution of convergent systems (Burov, 2007; Braun and Yamato, 2010), folding (Simpson, 2006; Collignon et al., 2014), rifting and faulting systems (Sacek et al., 2012; Andrés-Martínez et al., 2019; Theunissen and Huismans, 2019; Wolf et al., 2022a), subduction processes (Munch et al., 2022), and mountain belts (Willett, 1999; Thieulot et al., 2014; Ueda et al., 2015; Wolf et al., 2022b) through both 2D and 3D models. While numerical simulations offer powerful insights, fully 3D numerical models that couple thermo-mechanical processes with landscape processes in a self-consistent manner remain uncommon due to mismatches in spatial and temporal scales between the thermo-mechanical model and the landscape evolution model. On the spatial scale, most landscape evolution models are designed for length scales ranging from a few meters to several kilometers and require high resolution (Stock and Dietrich, 2006; Braun and Willett, 2013; Olive et al., 2014; Thieulot et al., 2014; Willett et al., 2014). In contrast, thermo-mechanical models are suited to much larger scales, spanning hundreds to thousands of kilometers, and typically operate at lower resolution than landscape models (Pusok and Kaus, 2015; Yang et al., 2020b; Stanković et al., 2023; Maiti et al., 2024). This characteristic necessitates the inclusion of horizontal advection in landscape models and may require the use of interpolation schemes. On the temporal scale, thermo-mechanical models usually adopt larger timesteps, ranging from a thousand to ten thousand years, while landscape evolution models use much smaller timesteps, which may require resetting timesteps in coupled models (Ueda et al., 2015).

The evolution of river systems is significantly influenced by variations in lateral tectonic structure and events, which 2D models cannot accurately capture. In contrast, 3D models offer a more realistic tectonic and river evolution events. More three-dimensional coupling methods need to be developed.

https://doi.org/10.5194/egusphere-2026-1170
Preprint. Discussion started: 24 March 2026

Our study presents a new coupling module that integrates the 3D thermo-mechanical code LaMEM with the landscape evolution code FastScape. This module operates stably and efficiently across various thermo-mechanical and surface processes. We evaluate the sensitivity of the coupling module in subduction-collision processes and continental extension scenarios. Next, we demonstrate how this coupling module can be applied to large-scale geodynamic problems.

2 Method

We integrated the 3D parallel thermo-mechanical numerical code LaMEM (Kaus et al., 2016; version 2.1.4) with the landscape evolution code FastScape (Braun and Willett, 2013; Yuan et al., 2019; version 2.8.4). This integrated module, LaScape 1.0, operates stably and efficiently across various spatial and temporal scales. It incorporates various grid schemes, including uniform, non-uniform, and dynamic grids (in which the grid spacing changes due to compression or extension). This module achieves a more realistic interaction between surface processes and tectonic events.

2.1 Thermo-mechanical model

LaMEM (Kaus et al., 2016) is a 3D thermo-mechanical numerical code that employs a finite difference staggered grid combined with the marker-in-cell technique. It solves the governing equations of momentum, mass, and energy conservation (1–3) using a multigrid approach:

$$-\frac{\partial P}{\partial x_i}+\frac{\partial \tau_{ij}}{\partial x_j}+\rho g_i=0\,, \tag{1}$$

$$\frac{1}{K}\frac{DP}{Dt}-\alpha\frac{DT}{Dt}+\frac{\partial v_i}{\partial x_i}=0\,, \tag{2}$$

$$\rho C_{\mathrm{p}}\left(\frac{\mathrm{D}T}{\mathrm{D}t}\right)=\frac{\partial}{\partial x_i}\left(\lambda\frac{\partial T}{\partial x_i}\right)+H\,, \tag{3}$$

where g_i are components of gravitational acceleration, P is pressure, ρ is density, τ_{ij} are components of deviatoric stress tensor, K is the bulk modulus, α is the thermal expansion coefficient, v_i are components of velocity, C_{p} is the effective isobaric heat capacity, λ is thermal conductivity, H is volumetric heat source, and $\frac{\mathrm{D}}{\mathrm{D}t}$ is the substantial time derivative.

The code incorporates the visco-elasto-plastic rheology, where the deviatoric strain rate consists of the following components:

https://doi.org/10.5194/egusphere-2026-1170
Preprint. Discussion started: 24 March 2026

$$\dot{\varepsilon}_{ij} = \dot{\varepsilon}_{ij}^{el} + \dot{\varepsilon}_{ij}^{diff} + \dot{\varepsilon}_{ij}^{disl} + \dot{\varepsilon}_{ij}^{pl} = \frac{\hat{\tau}_{ij}}{2G} + \eta_{diff}\tau_{ij} + \eta_{disl}(\tau_{II})^{n-1} + \dot{\lambda}\frac{\partial Q}{\partial \sigma_{ij}}, \quad (4)$$

where $\dot{\varepsilon}_{ij}^{\mathrm{el}}$, $\dot{\varepsilon}_{ij}^{\mathrm{diff}}$, $\dot{\varepsilon}_{ij}^{\mathrm{disl}}$, $\dot{\varepsilon}_{ij}^{\mathrm{pl}}$ are the elastic, diffusion, dislocation, and plastic strain rate, respectively. G is the elastic shear modulus, $\hat{\tau}_{ij} = \frac{\partial \tau_{ij}}{\partial t} + \tau_{ik}\omega_{kj} - \omega_{ik}\tau_{kj}$ is the Jaumann objective stress rate, $\omega_{ij} = \frac{1}{2}(\frac{\partial v_i}{\partial x_j} - \frac{\partial v_j}{\partial x_i})$ is the spin tensor. η_{diff} and η_{disl} are diffusion and dislocation constants, respectively. n is the power-law exponent for dislocation creep. τ_{II} is the square root of the second invariant of the deviatoric stress tensor. $\dot{\lambda}$ is the magnitude of the plastic strain rate, and Q is the plastic flow potential.

The creep flow law follows:

$$\eta_{\mathrm{diff,disl}} = \frac{1}{2}(\dot{\varepsilon}_{\mathrm{II}})^{\frac{1-n}{n}}(B_{\mathrm{N}})^{-\frac{1}{n}}\exp\left(\frac{E+PV}{nRT}\right), \quad (5)$$

where $\dot{\varepsilon}_{\mathrm{II}} = \sqrt{0.5\dot{\varepsilon}_{ij}^{\mathrm{vis}}\dot{\varepsilon}_{ij}^{\mathrm{vis}}}$ is the second invariant of the viscous strain rate tensor, B_{N}, E, V, n are experimentally determined flow law parameters, which represent pre-factor, stress exponent of dislocation creep, activation energy, and activation volume, respectively. R is the gas constant, P is the pressure, and T is the temperature.

Rock fails when the stress exceeds the yield stress (i.e., $\tau_{\mathrm{II}} > \tau_{\mathrm{y}}$), which follows the Drucker-Prager yielding criterion:

$$\tau_{\mathrm{y}} = P\sin(\theta) + C\cos(\theta), \quad (6)$$

where τ_{y} is the yield stress, C is the cohesion, θ is the effective friction angle, and P is the pressure.

Within each computational cell, the effective viscosity (η_{eff}) for nonlinear visco-elasto creep rheology is computed by numerically solving the scalar equation $r(\eta_{\mathrm{eff}})$ using a bisection method (Popov and Sobolev, 2008):

$$r(\eta_{\mathrm{eff}}) = \dot{\varepsilon}_{\mathrm{II}}^{*} - \frac{\tau_{\mathrm{II}}}{2G\Delta t} - \eta_{\mathrm{diff}}\tau_{\mathrm{II}} - \eta_{\mathrm{disl}}(\tau_{\mathrm{II}})^{n}, \quad (7)$$

https://doi.org/10.5194/egusphere-2026-1170
Preprint. Discussion started: 24 March 2026

$$\tau_{\mathrm{II}} = 2\eta_{\mathrm{eff}}\dot{\varepsilon}^{*}_{\mathrm{II}}\,, \tag{8}$$

The effective strain rate ($\dot{\varepsilon}^{*}_{ij}$) incorporates a term resulting from advected and rotated deviatoric history stress from the previous time step (τ^{*}_{ij}) as follows:

$$\dot{\varepsilon}^{*}_{ij} = \dot{\varepsilon}_{ij} + \frac{\tau^{*}_{ij}}{2G\Delta t}\,, \tag{9}$$

History stresses are advected via markers, followed by distance-based averaging of stress components within the control volumes of the staggered grid. Stress rotation is implemented through numerical integration of the Jaumann objective stress rate, ensuring asymptotically correct results for large finite time steps (Thielmann et al., 2015; Gerya, 2019).

When plastic failure occurs, the effective viscosity is directly computed through:

$$\eta_{\mathrm{eff}} = \frac{\tau_{\mathrm{y}}}{2\dot{\varepsilon}^{*}_{\mathrm{II}}}\,, \tag{10}$$

2.2 Landscape evolution model

Based on the special node ordering method and implicit solve structure, FastScape can efficiently and stably solve the equation governing long-term fluvial erosion and sediment deposition (Braun and Willett, 2013; Yuan et al., 2019). The equation is described as:

$$\frac{\partial h}{\partial t} = U - K_{\mathrm{f}}\tilde{p}^{\mathrm{m}}A^{\mathrm{m}}S^{\mathrm{n}} + \frac{G}{\tilde{p}A}\int_{A}\left(U - \frac{\partial h}{\partial t}\right)dA + K_{\mathrm{d}}\nabla^{2}h\,, \tag{11}$$

where h is topography, U is the rock uplift rate, A is the upstream catchment area (drainage area), S is the slope, m and n are the stream power exponents, K_{f} is the bedrock erodibility, K_{d} is the transport coefficient for hillslope diffusion, and D is a non-dimensional continental deposition coefficient. The dimensionless $\tilde{p}$ parameter represents any spatial or temporal variation in precipitation p relative to the mean precipitation rate. G is a non-dimensional deposition coefficient.

https://doi.org/10.5194/egusphere-2026-1170
Preprint. Discussion started: 24 March 2026

2.3 The coupling module

LaMEM and FastScape are coupled via a coupling module that exchanges information and stores necessary geomorphic data (Fig. 1). Due to the complexity of the thermo-mechanical equations, LaMEM utilizes a parallel approach based on PETSc to efficiently solve them across parallel computing clusters. In contrast, FastScape operates in a serial computation mode. We have included an information transceiver part that collects data from each parallel processor in LaMEM and integrates it for transmission to the primary processor (Fig. 1b). This primary processor handles surface processes and runs FastScape. The velocity and topography parameters (v_x, v_y, v_z, h) are exchanged between LaMEM and FastScape at the surface grid nodes without any loss of information. The landscape evolution model receives topography from the thermo-mechanical model at the first timestep and uses the previous topography field stored in the FastScape grid for iteration without re-receiving the topography data from LaMEM at every timestep during the landscape evolution. However, the velocity fields are received from LaMEM at every timestep in FastScape. After the calculation of landscape evolution, the updated topography field will be passed to LaMEM. We include horizontal advection in surface processes to simulate plate movement. A bilinear interpolation algorithm is used to produce more refined surface processes. Assuming the refined factor is n. Then, n-1 points are inserted at equal intervals between the two grid nodes of LaMEM, and their values are determined through bilinear interpolation. As a result, the grid resolution is increased by the refined factor n in both the x and y directions. Additionally, because of the mismatch between thermo-mechanical and geomorphic timesteps, the timesteps for calculating surface processes will be updated based on the initial step value set in the input file. When the user-defined maximum timestep in the landscape evolution model exceeds the final timestep of the thermo-mechanical model, the thermo-mechanical timestep will be applied for landscape evolution. Otherwise, the user-defined landscape evolution timestep will be utilized for iteration.

Due to the flexibility in selecting grid types in LaMEM, corresponding adjustments are required in FastScape. When using a non-uniform grid in LaMEM, the minimum grid spacing in LaMEM is used to create a higher resolution rectangular grid in FastScape. When there is a mismatch between the grids in FastScape and LaMEM, a bilinear interpolation scheme that uses the nearest 4 grid nodes is included to transfer values from LaMEM to FastScape, and vice versa. For a 2D thermo-mechanical model, an extended length is introduced to form an x-y surface in FastScape, in contrast to the original line along the x-direction or y-direction in LaMEM (Fig. 1c). All values used to initialize the model in FastScape are set according to this same principle: Each value on a line perpendicular to the original line in LaMEM is assigned the value of the corresponding point on the original line in LaMEM. After completing the geomorphic evolution at this time step, the average value along the extended line is calculated and returned to the corresponding grid in LaMEM.

No absolute conservation of rock mass is maintained during the evolution of the coupling model due to varying surface boundary conditions. Eroded mass can be potentially lost through the lateral boundaries without impacting the internal thermo-

https://doi.org/10.5194/egusphere-2026-1170
Preprint. Discussion started: 24 March 2026

mechanical mass. A fixed boundary results in a loss of all mass considered as sediment discharge, while a reflective boundary ensures strict conservation of mass.

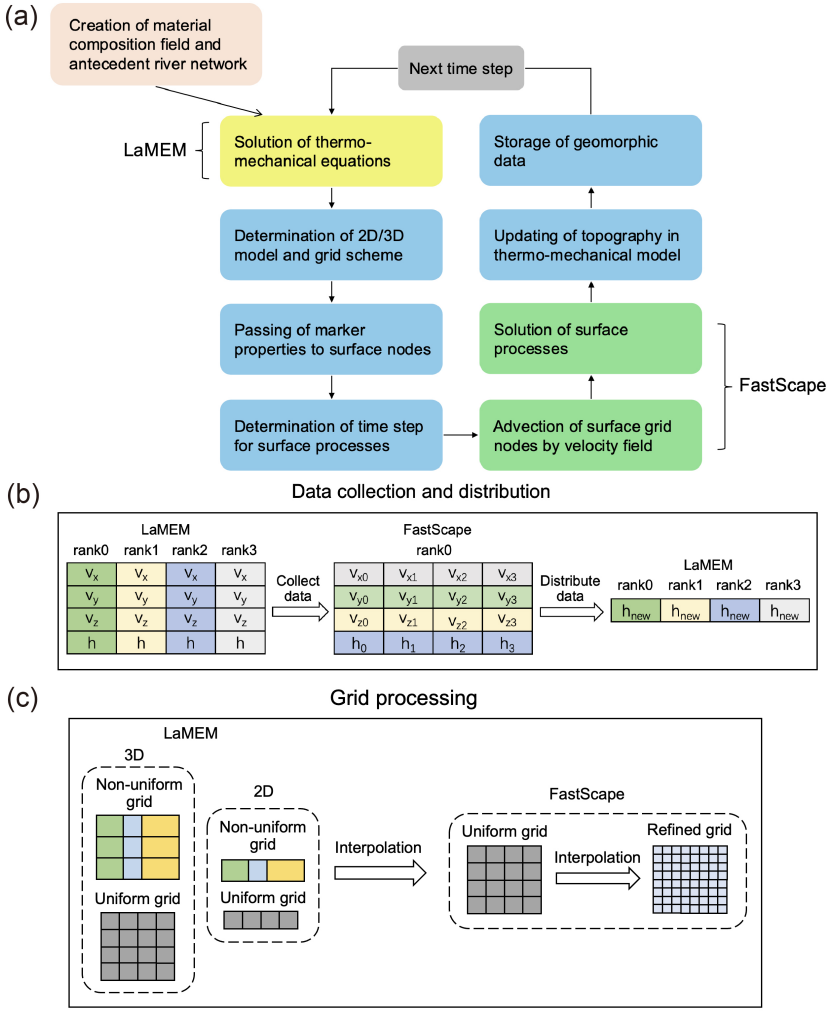

Figure 1: The operation process of the coupling module. (a) Flow chart for coupled computation with synchronous stepping. Steps with yellow background: thermo-mechanical calculation; green: surface processes calculation; blue: coupling module calculation. (b) The cartoon of the data collection and distribution module. The data collection and distribution module operates on rank 0. It collects data from other ranks to rank 0, then calls FastScape for calculation in rank 0. After the landscape evolution is calculated, the topography field is passed to LaMEM. (c) The cartoon of the grid processing module. Due to the diversity of LaMEM grid settings, the interpolation scheme is included to generate the uniform rectangular grid required for FastScape calculations, which are refined according to user requirements to achieve higher-precision geomorphic evolution.

https://doi.org/10.5194/egusphere-2026-1170
Preprint. Discussion started: 24 March 2026

3 Model implementation and examples

We construct different tectonic regimes to demonstrate our fully coupled model. Specifically, we design two sets of models: subduction-collision models and continental extension models. The subduction-collision models are designed on large spatial and temporal scales to investigate whether surface processes can influence long-term thermo-mechanical processes (e.g., subduction, collision, plume) at the mantle scale. In contrast, the continental extension focuses on a smaller spatial and temporal scale to determine whether the surface processes can affect short-term thermos-mechanical processes (e.g., earthquakes, faulting) at the crustal scale. The models with and without surface processes are shown for comparison. Additionally, we systematically test both thermo-mechanical and surface parameters to evaluate the stability and efficiency of the method across different tectonic configurations.

3.1 Oceanic subduction and continental collision

3.1.1 Initial model setting

Oceanic subduction and continental collision are fundamental processes in plate tectonics. These two processes significantly shape Earth's surface and interior (Gutscher et al., 2000; Martin-Short et al., 2016; Gordeev and Bergal-Kuvikas, 2022; Maiti et al., 2024). In this section, we establish a simple 3D thermo-mechanical-geomorphological model to investigate the evolution of subduction and collision processes both with and without surface processes. The model domain is 1,800 km × 600 km × 675 km (Fig. 2), resolved by the Eulerian mesh of 576 × 192 × 192 cells. The model is composed of a 650-km-long left continent, a 350-km-long ocean, and an 800-km-long right continent. The continents comprise a 20-km-thick upper crust, a 20-km-thick lower crust, and an 80-km-thick lithospheric mantle. The ocean comprises an 8-km-thick crust and a 90-km-thick lithospheric mantle. All rheological parameters are listed in Tables 1 and 2. The model is free-slip for all boundaries except the free-surface top boundary. A 15-km-thick "sticky-air" layer is used to mimic the internal free-surface condition in the finite difference scheme. We apply a constant pushing velocity on the subducting plate (5 cm yr^{-1}). A 15-km-thick weak zone between the subducting and overriding plate is used to initiate the subduction. The side boundaries have zero flux, and a linear temperature profile is employed with a fixed temperature of 0°C at the surface and 1630°C at the bottom. A linear strain weakening of the internal friction angle is used in the model, which linearly decreases by 90% between a strain of 0.01 and 0.05.

FastScape has the same domain as the tectonic model's plane (1,800 km × 600 km), and the resolution is finer than the thermo-mechanical (1152 × 384 cells) model. The stream power exponents are set to m = 0.4 and n = 1.0 (Yuan et al., 2019; 2022). All boundaries are open, where flux is allowed to pass.

https://doi.org/10.5194/egusphere-2026-1170
Preprint. Discussion started: 24 March 2026

Table 1: The rheological parameters used in numerical models.

Notation	Rheology	E (kJ mol^{-1})	V (cm^3 mol^{-1})	n	B_N (Pa^{-n} s^{-1})
A	Isoviscous	0	0	1	5×10^{-19}
B	Wet Quartzite[a]	154	0	2.3	1.55×10^{-17}
C	An$_{75}$ – plagioclase[a]	238	0	3.2	1.05×10^{-22}
D	Dry olivine[b]	530	15	3.5	6.22×10^{-16}
		375	5	1	1.5×10^{-9}
E	Isoviscous	0	0	1	5×10^{-20}

Flow laws used in numerical models are from experimental data: [a]Ranalli (1995), [b]Hirth and Kohlstedt (2003).

Table 2: Main material parameters in subduction-collision models.

Materials	ρ (kg m^{-3})	C (MPa)	ϕ (°)	K (W m^{-1} K^{-1})	H_r (W kg^{-1})	Rheology
Upper crust of continents	2700	10	10	2.5	3×10^{-10}	B
Lower crust of continents	2900	10	20	3.0	3×10^{-11}	C

https://doi.org/10.5194/egusphere-2026-1170
Preprint. Discussion started: 24 March 2026

Oceanic crust	2900	1	5	3.0	3×10^{-11}	B
Lithospheric mantle of continents	3300	10	30	3.5	6×10^{-12}	D
Lithospheric mantle of oceans	3300	10	30	3.5	6×10^{-12}	D
Sublithospheric mantle	3300	10	30	3.5	6×10^{-12}	D
Air	1	--	--	100	0	A
Weak zone	3200	--	--	3	0	E

For all rock types, the thermal expansivity $\alpha = 3\times10^{-5}$ K^{-1}, compressibility $\beta = 1\times10^{-11}$ Pa^{-1}, heat capacity $C_p = 1200$ J kg^{-1}

https://doi.org/10.5194/egusphere-2026-1170
Preprint. Discussion started: 24 March 2026

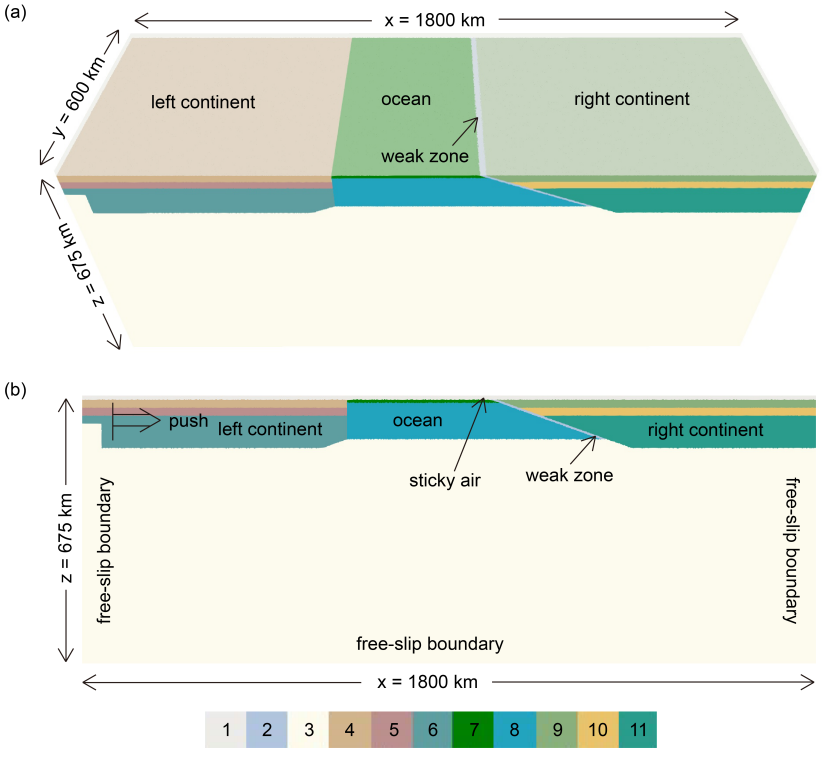

Figure 2: Initial model setup for subduction-collision models. (a) 3D view of the compositional field. (b) The vertical profile at y = 0 km. 1-sticky air; 2-weak zone; 3-sublithospheric mantle; 4-upper crust of left continent; 5-lower crust of left continent; 6-lithospheric mantle of left continent; 7-oceanic crust; 8-oceanic lithospheric mantle; 9-upper crust of right continent; 10-lower crust of right continent; 11-lithospheric mantle of right continent.

3.1.2 The evolution of the reference model

We ran two sets of models: with and without surface processes. Two stages could be reorganized in the evolution of the reference model (Fig. 3). Stage 1: *Oceanic subduction.* The subducting oceanic slab bends and subducts under the continuous convergence force, which causes a negative topography above the subducting oceanic slab. Some portions of oceanic crust enter the subducting channel, while others accumulate in the trench. Combined with a slight crustal shortening in the overriding slab near the trench, a small-scale positive topography forms on the overriding slab near the trench (Fig. 3a, b, d, and e). Stage 2: *Continental collision.* During continental collision, much of the crust accumulates near the convergence boundary. In contrast, the remaining continental lithosphere subducts due to the combined forces of convergence and slab pull from the oceanic slab. An orogenic wedge forms and extends, reaching a maximum elevation of ~5 km and an extensive range of ~300 km (Fig. 3c and f) because of crustal shortening and folding in both the subducting and overriding slabs. Compared to the

https://doi.org/10.5194/egusphere-2026-1170
Preprint. Discussion started: 24 March 2026

model without surface processes, the erosion and deposition processes do not significantly affect deep geodynamic processes but result in a slight topographic change. The topographic difference (equal to the elevation in the reference model without surface processes minus that in the model with surface processes) reveals a large-scale higher positive value at the edge of the subducting continent (~400-600 km), indicating a large-scale river erosional effect (Fig. 4c). Additionally, there are localized higher positive topographic differences near the rivers, specifically around 1300-1400 km, highlighting the small-scale roughness due to the fluvial erosion. While rivers play a role in tectonically stable zones, they do not significantly shape the orogenic wedge due to a balance between erosion processes and bedrock uplift. The middle bedrock erodibility used in the reference model results in a steeper slope in the orogenic wedge (Fig. 4).

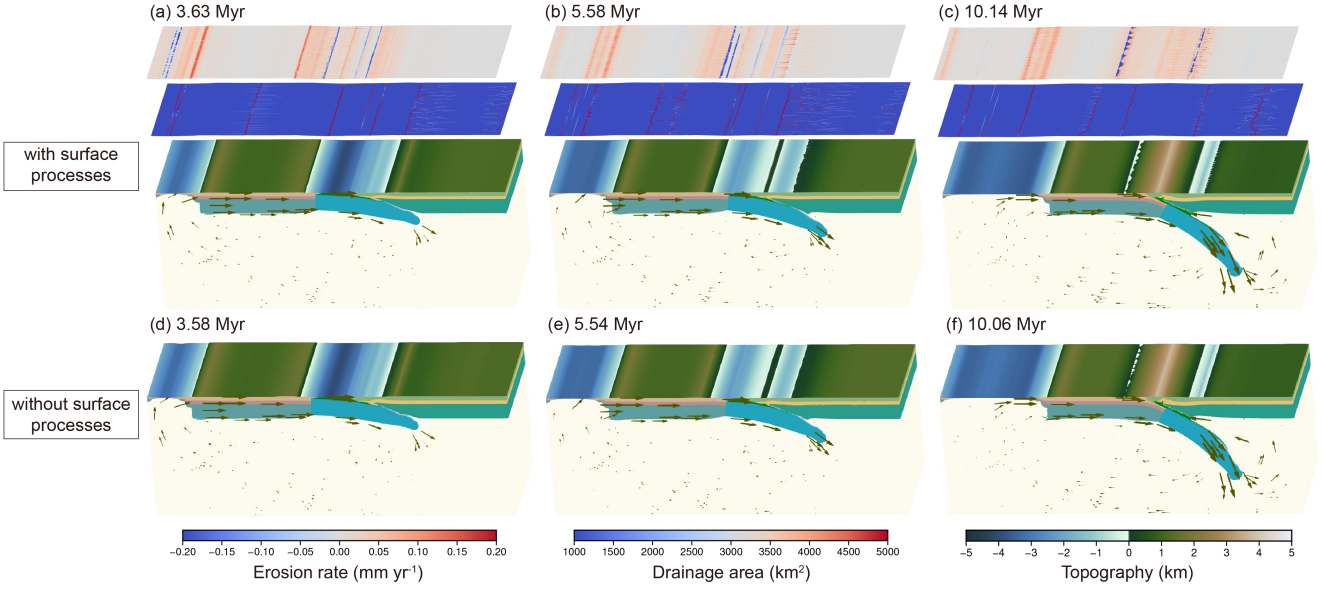

Figure 3: The evolution of the reference model for subduction-collision models with (a–c) /without (d–f) surface processes. For each panel, from top to bottom: erosion rate, drainage area, and composition field overlies with topographic elevation. The density difference between the lithospheric mantle and sublithosphere ($\Delta\rho$) is 0 kg m^{-3}. The convergence rate is 0 cm yr^{-1}. The flow laws of rocks are shown in Tables 1 and 2. The bedrock erodibility (K_f) is 1×10^{-6} m$^{0.2}$ yr^{-1}. The transport coefficient (K_d) is 1×10^{-2} m^2 yr^{-1}. The olive-green arrows show the velocity field. The colors of rock types are the same as in Fig. 2.

https://doi.org/10.5194/egusphere-2026-1170
Preprint. Discussion started: 24 March 2026

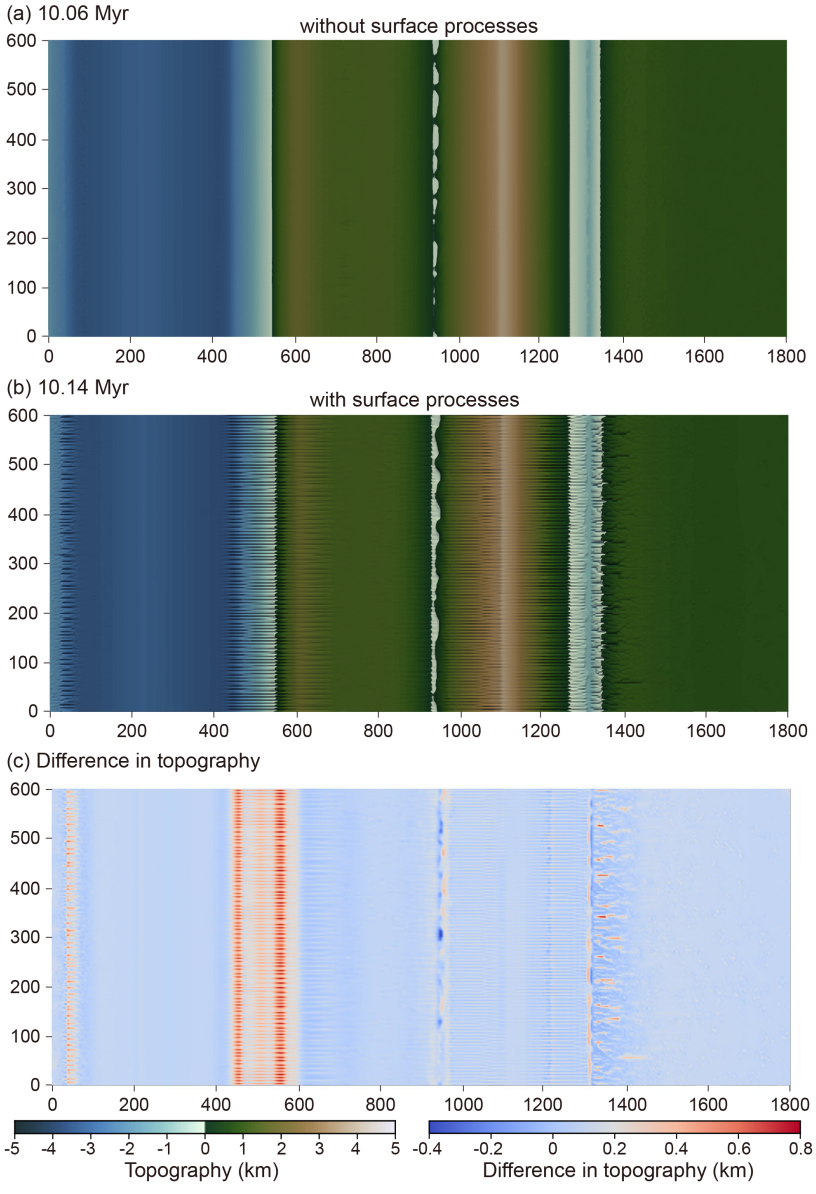

Figure 4: Comparison of reference model without/with surface processes for subduction-collision models. (a) The evolution of the reference model without surface processes. (b) The evolution of the reference model with surface processes. (c) The topographic difference in the reference model. The topographic difference is defined as the elevation in the reference model without surface processes minus that in the model with surface processes.

https://doi.org/10.5194/egusphere-2026-1170
Preprint. Discussion started: 24 March 2026

3.1.3 Parameter variations

We investigate the effects of thermo-mechanical parameters (density difference between the lithospheric mantle and sublithosphere ($\Delta\rho$) and convergence rate (V_c)) and surface parameters (bedrock erodibility K_f and transport coefficient K_d) on subduction-collision processes.

The $\Delta\rho$ affects the slab pull and further influences the subduction angle. When $\Delta\rho$ is less than 0, flat subduction occurs and causes a larger and higher orogenic wedge. There is a wide basin on the overriding slab that forms a large river system. Conversely, when $\Delta\rho$ increases to 0, steep subduction appears, leading to a smaller and lower orogenic wedge. A small basin forms on the overriding slab, leading to a smaller river system. When $\Delta\rho$ is larger than 0, the high slab pull causes the oceanic slab to break off, resulting in a relatively low basin situated between two orogenic wedges. An inland river forms within this basin. Besides, there is no obvious basin on the overriding slab (Fig. 5a–c).

The convergence rate determines the time required to achieve a certain convergence distance. A lower convergence rate allows more time for the subducting slab to adapt to the mantle flow and bend more, which results in a lower and smaller orogenic wedge due to longer erosional processes (Fig. 5d–f). However, the geometry of river systems has not changed significantly.

Although the bedrock erodibility does not significantly influence the geometry of the subducting slab, it primarily impacts the landscape. An increased bedrock erodibility leads to a lower and smaller orogenic wedge with steeper local slopes over long geological timescales. Additionally, higher bedrock erodibility leads to less positive topography and more tributaries of rivers due to the rapid erosion processes (Fig. 5g–i).

The transport coefficient does not largely affect the geometry of the subducting slab, but it changes the river systems and the scale of the orogenic wedge. A higher diffusion coefficient leads to a larger orogenic wedge. Besides, there are relatively larger river systems due to the smoother topography in the higher diffusion coefficient (Fig. 5j–l).

https://doi.org/10.5194/egusphere-2026-1170
Preprint. Discussion started: 24 March 2026

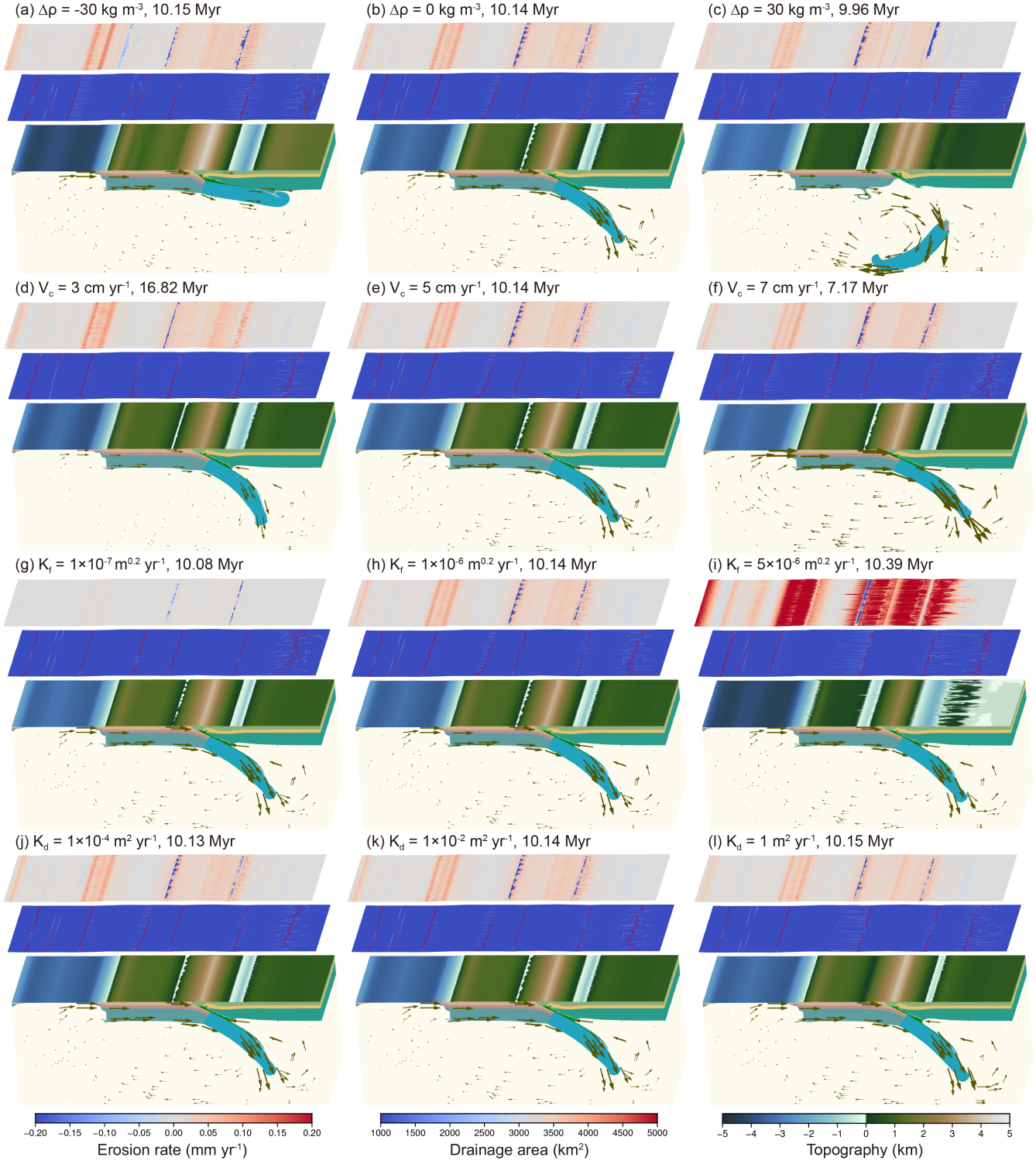

245

https://doi.org/10.5194/egusphere-2026-1170
Preprint. Discussion started: 24 March 2026

Figure 5: Parameters sensitive test of subduction-collision models. (a–c) Different $\Delta\rho$ from -30 kg m^{-3} to 30 kg m^{-3}. (d–f) Different convergence rates from 3 cm yr^{-1} to 7 cm yr^{-1}. (g–i) Different bedrock erodibilities from 1×10^{-7} $m^{0.2}$ yr^{-1} to 5×10^{-6} $m^{0.2}$ yr^{-1}. (j–l) Different diffusion coefficients vary from 1×10^{-4} m^2 yr^{-1} to 1 m^2 yr^{-1}. The olive-green arrows show the velocity field. The colors of rock types are the same as in Fig. 2. For each panel, from top to bottom: erosion rate, drainage area, and composition field overlies with topographic elevation.

3.2 Continental extension

3.2.1 Initial model setup

Continental extension directly impacts the lithosphere-asthenosphere system, resulting in increased rifting and volcanic activity (Corti et al., 2003; Corti, 2012). In this section, a small-scale 3D thermo-mechanics-geomorphological model is set to investigate the evolution of continental extension with and without surface processes. The model domain is 200 km × 100 km × 68 km (Fig. 6), resolved by the Eulerian mesh of 128 × 64 × 32 cells. A dynamic grid is used to adapt to the background strain rate. A 20-km-thick upper crust and a 20-km-thick lower crust are included in this model. All the rheological parameters are presented in Tables 1 and 3. The model is free-slip for all boundaries except the free-surface top boundary. An 8-km-thick "sticky-air" layer is used to mimic the free-surface condition in the finite difference scheme. An extensional strain rate (7.92×10^{-16} s^{-1}, corresponding to 0.25 cm yr^{-1}) is applied. The side boundaries have zero flux, and a linear temperature profile is employed with a fixed temperature of 0°C at the surface and 650°C at the bottom. A linear strain weakening of the friction angle is also applied as the subduction-collision model.

FastScape has the same domain as the tectonic model (200 km × 100 km) but employs a finer resolution than the thermo-mechanical (256 × 128 cells) model. The stream power exponents are set to m = 0.4 and n = 1.0 (Yuan et al., 2019, 2022). All the boundaries are open, where flux is allowed to pass. To eliminate the influence of random noise when comparing the influence of the surface processes, neither the thermos-mechanical model nor the landscape evolution model includes random noise.

Table 3: Main material parameters in continental extension models.

Materials	ρ (kg m^{-3})	C (MPa)	ϕ (°)	K (W m^{-1} K^{-1})	H_r (W kg^{-1})	Rheology
Upper crust	2700	10	10	2.5	3×10^{-10}	B

https://doi.org/10.5194/egusphere-2026-1170
Preprint. Discussion started: 24 March 2026

Lower crust	2900	10	20	3.0	3×10^{-11}	C
Air	1	--	--	100	0	A

For all rock types, the thermal expansivity $\alpha = 3\times10^{-5}$ K^{-1}, compressibility $\beta = 1\times10^{-11}$ Pa^{-1}, heat capacity $C_p = 1200$ J kg^{-1}

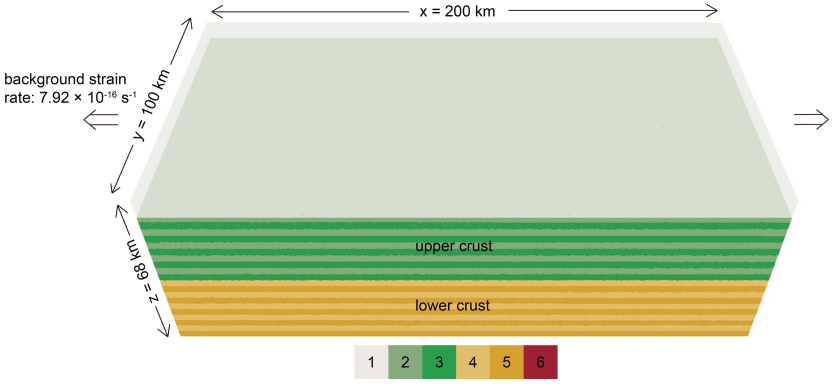

Figure 6: Initial model setup for continental extension models. A force is applied perpendicular to the z-y face at the left and right sides to stretch the rocks, resulting in a background strain rate of 7.92×10^{-16} s^{-1} (corresponding to 0.25 cm yr^{-1}). 1-sticky air; 2-upper crust; 3-upper crust; 4-lower crust; 5-lower crust; 6-sediment.

3.2.2 The evolution of continental extension model with/without surface processes with high bedrock erodibility

A similar thermos-mechanical evolution occurs under extensional forces, both with/without surface processes with high bedrock erodibility. Initially, there are no significant shear zones within the crust and no significant topography (Fig. 7a and c). However, some conjugate faults form as strain accumulates while the upper and lower crust flows to accommodate the extension. Due to variations in density and rheology, parts of the lower crust rise while the upper crust thins in the same area, resulting in a fold-like structure. When there doesn't include surface processes, positive topography develops where the crust uplifts, while negative topography develops where the crust sinks downward (Fig. 7d). However, when there include surface processes with very high bedrock erodibility equals to 1×10^{-4} m$^{0.2}$ yr^{-1}, very rapid erosion processes has led to an overall negative topography lower than -3 km (Fig. 7b). The surface processes slightly change the crustal stress distribution and local

https://doi.org/10.5194/egusphere-2026-1170
Preprint. Discussion started: 24 March 2026

crustal flow, and there is a slower crustal flow in the left part and a faster crustal flow in the right part. These changes in topography further alter the distribution of shear zones (Fig. 7b and d).

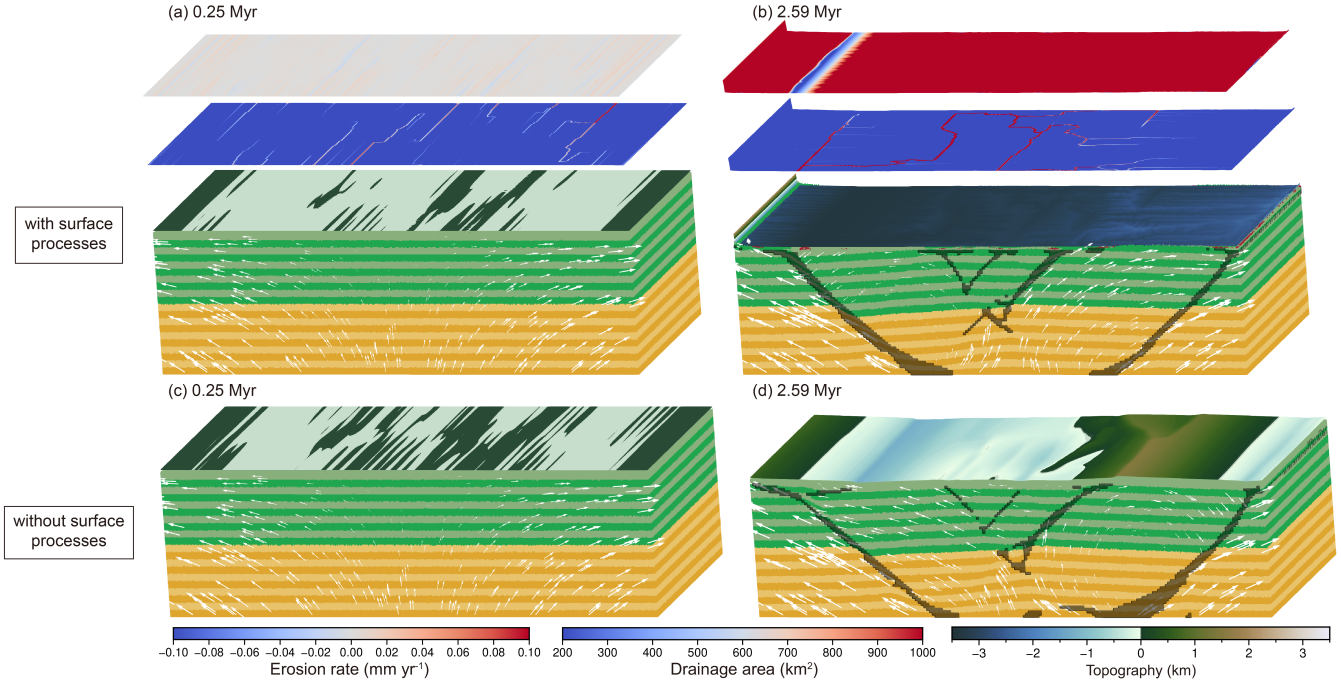

Figure 7: The evolution of models for continental extension with (a–b) /without (c–d) surface processes. (a–b) The evolution of the model with surface processes with bedrock erodibility equals to 1×10^{-4} $m^{0.2}$ yr^{-1}. (c–d) The evolution of the model without surface processes. For each panel, from top to bottom: erosion rate, drainage area, and composition field overlies with topographic elevation. The white arrows show the movement of the crust. The black lines indicate where the strain rate is greater than 3×10^{-15} s^{-1}. The colors of rock types are the same as in Fig. 6.

3.2.3 Parameter studies

We investigate how thermos-mechanical parameters, specifically the background strain rate (V_e) and the rheology of the lower crust, as well as surface parameters like the bedrock erodibility (K_f) and the transport coefficient (K_d), affect the evolution of continental extension.

The background strain rate plays a significant role in forming shear zones and influencing the rate of rock deformation. A higher half extensional rate results in a larger scale of shear zones and greater crustal deformation at similar extension distances.

https://doi.org/10.5194/egusphere-2026-1170
Preprint. Discussion started: 24 March 2026

Additionally, increased velocity of crustal movement leads to greater amplitudes and higher variations in topography (Fig. 8a–c).

The rheology of the lower crust reflects its ability to resist deformation. With a weak lower crust, the deformation caused by extensional forces can be absorbed more effectively, leading to a lower topography. Conversely, as the strength of the lower crust increases, the number of shear zones decreases, resulting in more deformation concentrated in the upper crust. This concentration causes a greater variation in height (Fig. 8d–f).

The bedrock erodibility primarily affects surface processes and alters shear zones due to gravitational isostasy. An increased bedrock erodibility results in less positive topography due to the rapid erosion processes (Fig. 8g–i), therefore slightly changes the crustal flow and stress distribution.

The transport coefficient affects the smoothness of the topography. A higher diffusion coefficient results in a smoother topography (Fig. 8j–l).

Model results show that thermos-mechanical parameters and the bedrock erodibility affect the distribution of shear zones and topography. The river systems mainly develop around the transition zones between positive and negative topography. More discrete positive terrain has led to the development of more rivers.

https://doi.org/10.5194/egusphere-2026-1170
Preprint. Discussion started: 24 March 2026

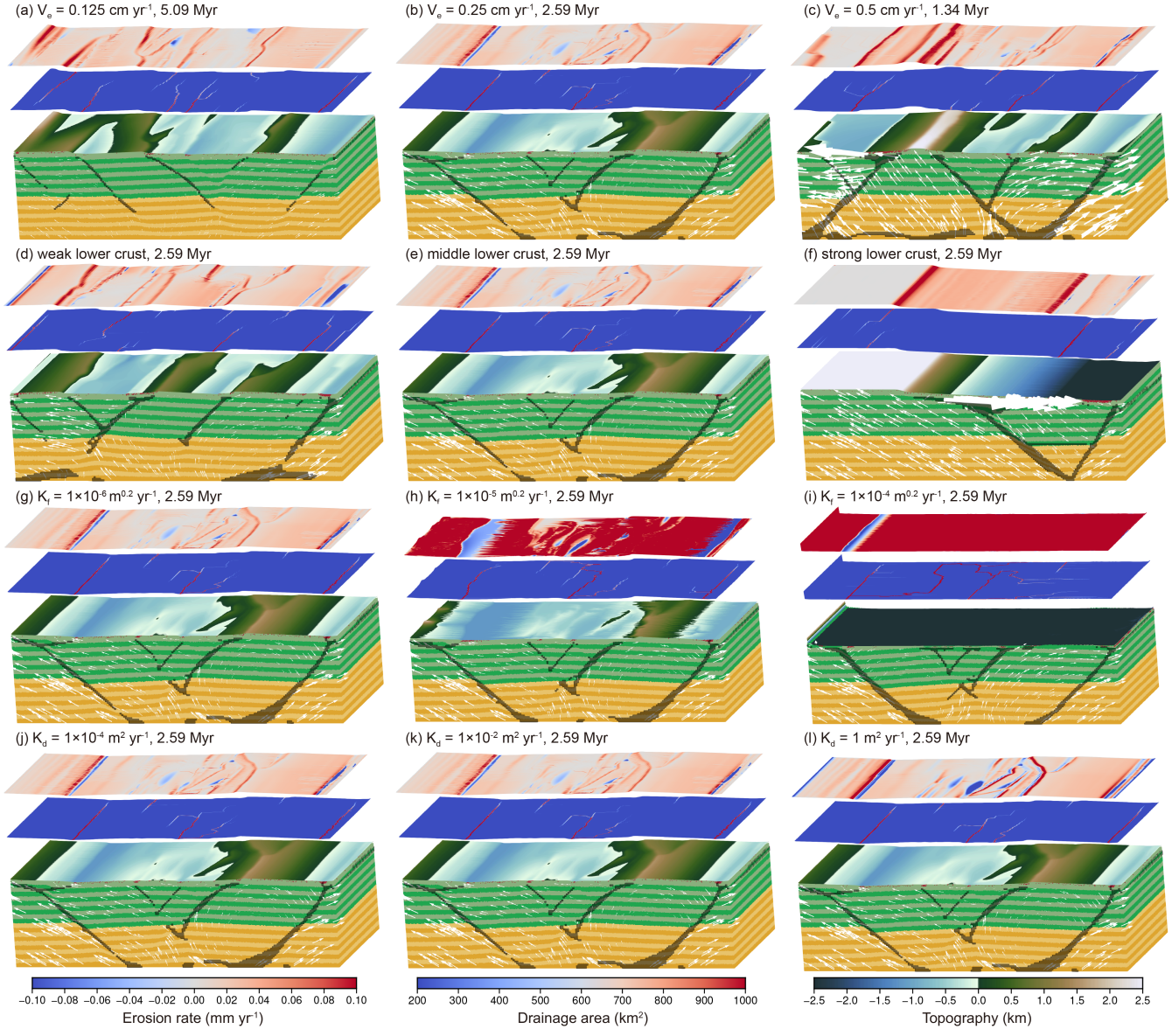

Figure 8: Parameters sensitive test of continental extension models. (a–c) Different half extensional rates from 0.125 cm yr^{-1} to 0.5 cm yr^{-1}. (d–f) Different rheology of the lower crust. The rheology flow used in this test: weak lower crust – quartz diorite (Carter and Tsenn, 1987), middle lower crust – An$_{75}$ – plagioclase (Ranalli, 1995), strong lower crust – mafic granulite (Ranalli, 1995). (g–i) Different bedrock erodibilities from 1×10^{-6} m$^{0.2}$ yr^{-1} to 1×10^{-4} m$^{0.2}$ yr^{-1}. (j–l) Different diffusion coefficient from 1×10^{-4} m^2 yr^{-1} to 1 m^2 yr^{-1}. The white arrows show the movement of the crust. The black lines indicate where

https://doi.org/10.5194/egusphere-2026-1170
Preprint. Discussion started: 24 March 2026

the strain rate is greater than 3×10^{-15} s^{-1}. The colors of rock types are the same as in Fig. 6. For each panel, from top to bottom: erosion rate, drainage area, and composition filed overlies with topographic elevation.

4 Discussion

The proposed approach effectively captures the interaction between tectonic deformation and surface processes, accommodating various underlying forcing mechanisms, grid settings, and deformation processes. The influence of fully coupled models on landscape and geodynamic evolution is demonstrated by comparing the reference model with and without surface processes (Figs. 3, 4, and 7). The most pronounced differences between models with and without surface processes are observed when comparing the no-erosion reference model with high erodibility cases, which leads to changes in topography, the distribution of shear zones and the crustal flow. Our full-scale coupling module further demonstrates the advantages of using fully coupled 3D models, as lateral variations in uplift and erosion occur along the strike of the main structure, which cannot be captured in 2D coupling models.

The tectonic events significantly shape the landscape, while the landscape also changes the stress field, crustal flow, and fault and seismic activity through gravitational isostasy (Zeitler et al., 2001; Liu et al., 2009; Wolf et al., 2022a; Wolf et al., 2022b; Li et al., 2025). Increasing attention is being given to the interaction between tectonic activity and surface processes.

We design two models for different temporal and spatial scales. Subduction-collision models are designed for a large temporal scale (>1 Myr) and large spatial scale (reaching the depth of the mantle transition zone). In contrast, continental extension models are designed for a relatively small temporal scale (faulting activity) and small spatial scale (crustal depth). Model results indicate that the impact of surface processes on geodynamic processes is limited to relatively small spatial scales. For instance, erosion and deposition affect crustal flow and further alter the distribution of shear zones (Figs. 7 and 8), which is also recognized in the previous research. Yang et al. (2023) demonstrate that rapid erosion causes the lower crust to flow upward. Wolf et al. (2022a) suggest that efficient surface processes lead to changes in fault propagation and segmentation. However, although surface processes significantly affect the topography, they do not notably impact deeper geodynamic processes, such as the geometry of subducting plates and mantle flow, even at high bedrock erodibility. The surface processes only change the geometry of the orogenic wedge and the appearance of basins (Figs. 3 and 5). Besides, rapid erosion may cause a higher height variation over a short time (compare Fig. 8g with 8h) unless the erosion process has removed all the positive topography. However, rapid erosion will cause a relatively lower height variation in the long term due to the balance of tectonic uplift and the gravitational isostasy caused by erosion-deposition processes (compare Fig. 5g with 5i).

https://doi.org/10.5194/egusphere-2026-1170
Preprint. Discussion started: 24 March 2026

5 Conclusions

Our new coupling module couples the thermo-mechanical code LaMEM with the landscape evolution code FastScape and could operate efficiently and stably. Various tectonic regimes, such as continental extension, oceanic subduction, and continental collision, can converge quickly and produce results. Model results show the influence of surface processes on geodynamic processes at different temporal and spatial scales. Our approach provides robust, quantitative support for the significant connection between deep tectonics and surface processes.

Code availability. The scripts and model inputs reported in this paper are available from Zenodo (https://doi.org/10.5281/zenodo.18834695, Luo et al., 2026) under the Creative Commons Attribution 4.0 International licence.

Data availability. There is no data used or generated in this study.

Author contributions. With guidance from JFY, BK, AP, XPY, and LZ, LY led the coupling of the model, implementing the representation of thermo-mechanics-surface interactions, model simulations, and results analysis. LY initially drafted the paper, with significant contributions from JFY, BK, AP, XPY, and LZ. SHL helped with the comparison of model results and ran some simulations through another coupling module, ASPECT-FastScape. All co-authors contributed to the paper review and editing.

Financial support. This study was supported by the National Natural Science Foundation of China (42488201), the Strategy Priority Research Program (Category B) of the Chinese Academy of Sciences (XDB0710000), and the National Key R&D Program of China (2025YFF0811502). This is a contribution to the project of Theory of Hydrocarbon Enrichment under Multi-Spheric Interactions of the Earth (THEMSIE).

Competing interests. I declare that I or my co-authors have competing interests as follows: At least one of the (co-)authors is a member of the editorial board of Geoscientific Model Development.

https://doi.org/10.5194/egusphere-2026-1170
Preprint. Discussion started: 24 March 2026

References

Andrés-Martínez, M., P´erez-Gussiny´e, M., Armitage, J., and Morgan, J.P.: Thermomechanical implications of sediment transport for the architecture and evolution of continental rifts and margins, Tectonics, 38, 641–665, https://doi.org/10.1029/2018TC005346, 2019.

Beaumont, C., Jamieson, R. A., Nguyen, M. H., and Lee, B.: Himalayan tectonics explained by extrusion of a low-viscosity crustal channel coupled to focused surface denudation, Nature, 414, 738–742, https://doi.org/10.1038/414738a, 2001.

Bettinelli, P., Avouac, J. P., Flouzat, M., Bollinger, L., Ramillien, G., Rajaure, S., and Sapkota, S.: Seasonal variations of seismicity and geodetic strain in the Himalaya induced by surface hydrology, Earth Planet. Sci. Lett., 266, 332–344, https://doi.org/10.1016/j.epsl.2007.11.021, 2008.

Bishop, P.: Long-term landscape evolution: linking tectonics and surface processes, Earth Surf. Proc. Land., 32, 329–365, https://doi.org/10.1002/esp.1493, 2007.

Borgohain, B., Mathew, G., Salvi, D., Harbola, D., and Rai, P.: Spatial-temporal variation in erosion rate of Lohit Bomi-Chayu Batholith around eastern Himalayan Syntaxis (SE of the Namche Barwa Massif), Tectonics, 44, e2024TC008507, https://doi.org/10.1029/2024TC008507, 2025.

Braun, J. and Willett, S.D.: A very efficient O(N), implicit and parallel method to solve the stream power equation governing fluvial incision and landscape evolution, Geomorphology, 180, 170–179, https://doi.org/10.1016/j.geomorph.2012.10.008, 2013.

Braun, J. and Yamato, P.: Structural evolution of a three-dimensional, finite-width crustal wedge, Tectonophysics, 484, 181–192, https://doi.org/10.1016/j.tecto.2009.08.032, 2010.

Braun, J.: The many surface expressions of mantle dynamics, Nat. Geosci., 3, 825–833, https://doi.org/10.1038/ngeo1020, 2010.

Burov, E. and Cloetingh, S.: Erosion and rift dynamics: new thermomechanical post-rift evolution of extensional basins, Earth Planet. Sci. Lett., 150, 7–26, https://doi.org/10.1016/S0012-821X(97)00069-1, 1997.

Burov, E. and Gerya, T.: Asymmetric three-dimensional topography over mantle plumes, Nature, 513, 85–89, https://doi.org/10.1038/nature13703, 2014.

Burov, E.: Coupled lithosphere-surface processes in collision context, Thrust Belts and Foreland Basins, 3–40, https://doi.org/10.1007/978-3-540-69426-7_1, 2007.

Carter, N. L. and Tsenn, M. C.: Flow properties of continental lithosphere, Tectonophysics, 136, 27–63, https://doi.org/10.1016/0040-1951(87)90333-7, 1987.

Castelltort, S., Goren, L., Willett, S.D., Champagnac, J.-D., Herman, F., and Braun, J.: River drainage patterns in the New Zealand Alps primarily controlled by plate tectonic strain, Nat. Geosci., 5, 744–748, https://doi.org/10.1038/ngeo1582, 2012.

https://doi.org/10.5194/egusphere-2026-1170
Preprint. Discussion started: 24 March 2026

Clark, M.K., Schoenbohm, L.M., Royden, L.H., Whipple, K.X., Burchfiel, B.C., Zhang, X., Tang, W., Wang, E., and Chen, L.: Surface uplift, tectonics, and erosion of eastern Tibet from large-scale drainage patterns, Tectonics, 23, https://doi.org/10.1029/2002TC001402, 2004.

Cloetingh, S. and Willett, S.D.: TOPO-EUROPE: understanding of the coupling between the deep Earth and continental topography, Tectonophysics, 602, 1–14, https://doi.org/10.1016/j.tecto.2013.05.023, 2013.

Collignon, M., Kaus, B., May, D., and Fernandez, N.: Influences of surface processes on fold growth during 3-d detachment folding, Geochem. Geophys. Geosyst., 15, 3281–3303, https://doi.org/10.1002/2014GC005450, 2014.

Corti, G., Bonini, M., Conticelli, S., Innocenti, F., Manetti, P., and Sokoutis, D.: Analogue modelling of continental extension: a review focused on the relations between the patterns of deformation and the presence of magma, Earth Sci. Rev., 63, 169–247, https://doi.org/10.1016/S0012-8252(03)00035-7, 2003.

Corti, G.: Evolution and characteristics of continental rifting: Analog modeling-inspired view and comparison with examples from the East African Rift System, Tectonophysics, 522, 1–33, https://doi.org/10.1016/j.tecto.2011.06.010, 2012.

Gao, S. S., Silver, P. G., Linde, A. T., and Sacks, I. S.: Annual modulation of triggered seismicity following the 1992 Landers earthquake in California, Nature, 406, 500–504, https://doi.org/10.1038/35020045, 2000.

Gerya, T. V. (Eds.): Introduction to numerical geodynamic modelling (2nd ed.), Cambridge University Press, ISBN 9781107143142, 2019.

Gordeev, E. I., and Bergal-Kuvikas, O. V.: Structure of the subduction zone and volcanism in Kamchatka, Dokl. Earth Sci., 502, 21–24, https://doi.org/10.1134/S1028334X22020088, 2022.

Gutscher, M. A., Spakman, W., Bijwaard, H., and Engdahl, E. R.: Geodynamics of flat subduction: Seismicity and tomographic constraints from the Andean margin, Tectonics, 19, 814–833, https://doi.org/10.1029/1999TC001152, 2000.

Heki, K.: Snow load and seasonal variation of earthquake occurrence in Japan, Earth Planet. Sci. Lett., 207, 159–164, https://doi.org/10.1016/S0012-821X(02)01148-2, 2003.

Hirth, G., and Kohlstedf, D.: Rheology of the upper mantle and the mantle wedge: A view from the experimentalists. Geophysical monograph-american geophysical union, 138, 83–106, 2003.

Kaus, B.J., Popov, A. A., Baumann, T., Pusok, A., Bauville, A., Fernandez, N., and Collignon, M.: Forward and inverse modelling of lithospheric deformation on geological timescales, Proceedings of nic symposium, 48, 978–983, 2016.

Koons, P. O., Zeitler, P. K., Hallet, B., Shroder, J., and Owen, L. A.: Tectonic aneurysms and mountain building, Treatise on geomorphology, 5, 318–349, 2013.

Li, K., Brune, S., Erdős, Z., Yuan, X., Glerum, A., Berndt, C., and Haas, P.: Pre-rift orogenic erosion facilitates the exhumation of lower crust at rifted margins, Geophys. Res. Lett., 52, e2024GL113543, https://doi.org/10.1029/2024GL113543, 2025.

Liu, C., Linde, A. T., and Sacks, I. S.: Slow earthquakes triggered by typhoons, Nature, 459, 833–836, https://doi.org/10.1038/nature08042, 2009.

Luo, Y., Yang, J., Kaus, B. J. P., Popov, A. A., Liu, S., Yuan, X., and Zhao, L.: The source code of the coupling module and input files (1.0.0), Zenodo [code], https://doi.org/10.5281/zenodo.18834695, 2026.

https://doi.org/10.5194/egusphere-2026-1170
Preprint. Discussion started: 24 March 2026

Maiti, G., Koptev, A., Baville, P., Gerya, T., Crosetto, S., and Andrić-Tomašević, N.: Topography response to horizontal slab tearing and oblique continental collision: Insights from 3D thermomechanical modelling, J. Geophys. Res. Solid Earth, 129, e2024JB029385, https://doi.org/10.1029/2024JB029385, 2024.

Martin-Short, R., Allen, R. M., and Bastow, I. D.: Subduction geometry beneath south central Alaska and its relationship to volcanism, Geophys. Res. Lett., 43, 9509–9517, https://doi.org/10.1002/2016GL070580, 2016.

Molnar, P., England, P., and Martinod, J.: Mantle dynamics, uplift of the Tibetan Plateau, and the Indian monsoon, Rev. Geophys, 31, 357–396, https://doi.org/10.1029/93RG02030, 1993.

Munch, J., Ueda, K., Schnydrig, S., May, D. A., and Gerya, T. V.: Contrasting influence of sediments vs surface processes on retreating subduction zones dynamics, Tectonophysics, 836, 229410, https://doi.org/10.1016/j.tecto.2022.229410, 2022.

Olive, J.-A., Behn, M.D., and Malatesta, L.C.: Modes of extensional faulting controlled by surface processes, Geophys. Res. Lett., 41, 6725–6733, https://doi.org/10.1002/2014GL061507, 2014.

Popov, A. A., and Sobolev, S. V.: Slim3d: A tool for three-dimensional thermomechanical modeling of lithospheric deformation with elasto-visco-plastic rheology, Phys. Earth Planet. Inter., 171, 55–75, https://doi.org/10.1016/j.pepi.2008.03.007, 2008.

Pusok, A. E., and Kaus, B. J.: Development of topography in 3-D continental-collision models, Geochem. Geophy. Geosy., 16, 1378-1400, https://doi.org/10.1002/2015GC005732, 2015.

Ranalli, G. (Eds.): Rheology of the Earth, Springer Science & Business Media, ISBN 9780412546709, 1995.

Replumaz, A., San José, M., Margirier, A., van Der Beek, P., Gautheron, C., Leloup, P.H., Ou, X., Kai, C., Wang, G.C., Zhang, Y.Z., and Valla, P.G.: Tectonic control on rapid late Miocene—quaternary incision of the Mekong River Knickzone, southeast Tibetan Plateau, Tectonics, 39, e2019TC005782, https://doi.org/10.1029/2019TC005782, 2020.

Sacek, V., Braun, J., and van der Beek, P.: The influence of rifting on escarpment migration on high elevation passive continental margins, J. Geophys. Res. Solid Earth, 117, http://dx.doi.org/10.1029/2011JB008547, 2012.

Simpson, G. D.: Modelling interactions between fold–thrust belt deformation, foreland flexure and surface mass transport, Basin Res., 18, 125-143, https://doi.org/10.1111/j.1365-2117.2006.00287.x, 2006.

Stanković, N., Gerya, T., Cvetkov, V., and Cvetković, V.: Did the Western and the Eastern Vardar ophiolites originate through a single intra-oceanic subduction? Insight from numerical modelling, Gondwana Res., 124, 124-140, https://doi.org/10.1016/j.gr.2023.07.005, 2023.

Stock, J.D. and Dietrich, W.E.: Erosion of steepland valleys by debris flows, Geol. Soc. Am. Bull., 118, 1125–1148, https://doi.org/10.1130/B25902.1, 2006.

Theunissen, T. and Huismans, R.S.: Long-term coupling and feedback between tectonics and surface processes during non-volcanic rifted margin formation, J. Geophys. Res. Solid Earth, 124, 12323–12347, https://doi.org/10.1029/2018JB017235, 2019.

https://doi.org/10.5194/egusphere-2026-1170
Preprint. Discussion started: 24 March 2026

Thielmann, M., Kaus, B. J., and Popov, A. A.: Lithospheric stresses in Rayleigh–Benard convection: effects of a free surface and a viscoelastic Maxwell rheology, Geophysical Supplements to the Monthly Notices of the Royal Astronomical Society, 203, 2200-2219, https://doi.org/10.1093/gji/ggv436, 2015.

Thieulot, C., Steer, P., and Huismans, R. S.: Three-dimensional numerical simulations of crustal systems undergoing orogeny and subjected to surface processes, Geochem. Geophys. Geosyst., 15, 4936–4957, https://doi.org/10.1002/2014GC005490, 2014.

Ueda, K., Willett, S.D., Gerya, T., and Ruh, J.: Geomorphological-thermo-mechanical modeling: application to orogenic wedge dynamics, Tectonophysics, 659, 12–30, https://doi.org/10.1016/j.tecto.2015.08.001, 2015.

Whipple, K. X.: The influence of climate on the tectonic evolution of mountain belts, Nat. Geosci, 2, 97-104, https://doi.org/10.1038/ngeo413, 2009.

Willett, S. D., McCoy, S. W., Perron, J. T., Goren, L., and Chen, C. Y.: Dynamic reorganization of river basins, Science, 343, 1248765, https://doi.org/10.1126/science.1248765, 2014.

Willett, S. D.: Orogeny and orography: The effects of erosion on the structure of mountain belts, J. Geophys. Res. Solid Earth, 104, 28957-28981, https://doi.org/10.1029/1999JB900248, 1999.

Wolf, L., Huismans, R. S., Wolf, S. G., Rouby, D., and May, D. A.: Evolution of rift architecture and fault linkage during continental rifting: Investigating the effects of tectonics and surface processes using lithosphere-scale 3D coupled numerical models, J. Geophys. Res. Solid Earth, 127, e2022JB024687, https://doi.org/10.1029/2022JB024687, 2022a.

Wolf, S. G., Huismans, R. S., Braun, J., and Yuan, X.: Topography of mountain belts controlled by rheology and surface processes, Nature, 606, 516-521, https://doi.org/10.1038/s41586-022-04700-6, 2022b.

Xue, L., Moucha, R., Scholz, C. A., and Naliboff, J.: Sedimentation and deformation in oblique continental rifts: The role of climate-tectonic interactions, Earth Planet. Sci. Lett, 669, 119565, https://doi.org/10.1016/j.epsl.2025.119565, 2025.

Yang, J., Cao, W., Yuan, X., and Yang, J.: Erosion-Driven Isostatic Flow and Crustal Diapirism: Analytical and Numerical Models with Implications for the Evolution of the Eastern Himalayan Syntaxis, Southern Tibet, Tectonics, 42, e2022TC007717, https://doi.org/10.1029/2022TC007717, 2023.

Yang, J., Kaus, B.J., Li, Y., Leloup, P.H., Popov, A.A., Lu, G., Wang, K., and Zhao, L.: Lower crustal rheology controls the development of large offset strike-slip faults during the Himalayan-Tibetan orogeny, Geophys. Res. Lett., 47, e2020GL089435, https://doi.org/10.1029/2020GL089435, 2020b.

Yang, R., Suhail, H.A., Gourbet, L., Willett, S.D., Fellin, M.G., Lin, X., Gong, J., Wei, X., Maden, C., Jiao, R., and Chen, H.: Early Pleistocene drainage pattern changes in Eastern Tibet: Constraints from provenance analysis, thermochronometry, and numerical modelling, Earth Planet. Sci. Lett., 531, 115955, https://doi.org/10.1016/j.epsl.2019.115955, 2020a.

Yuan, X. P., Braun, J., Guerit, L., Rouby, D., and Cordonnier, G.: A new efficient method to solve the stream power law model taking into account sediment deposition, J. Geophys. Res. Earth Surface, 124, 1346–1365, https://doi.org/10.1029/2018JF004867, 2019.

https://doi.org/10.5194/egusphere-2026-1170
Preprint. Discussion started: 24 March 2026

Yuan, X. P., Guerit, L., Braun, J., Rouby, D., and Shobe, C. M.: Thickness of fluvial deposits records climate oscillations, J. Geophys. Res. Solid Earth, 127, e2021JB023510, https://doi. org/10.1029/2021JB023510, 2022.

Yuan, X., Li, Y., Brune, S., Li, K., Pons, M., and Wolf, S.G.: Coordination between deformation, precipitation, and erosion during orogenic growth, Nat. Commun., 15, 10362, https://doi.org/10.1038/s41467-024-54690-4, 2024.

Zeitler, P.K., Meltzer, A.S., Koons, P.O., Craw, D., Hallet, B., Chamberlain, C.P., Kidd, W.S., Park, S.K., Seeber, L., Bishop, M., and Shroder, J.: Erosion, Himalayan geodynamics, and the geomorphology of metamorphism, Gsa Today, 11, 4-9, 2001.